

**SIMULTANEOUS RECONSTRUCTION AND SEGMENTATION
WITH THE MUMFORD-SHAH FUNCTIONAL FOR ELECTRON
TOMOGRAPHY**

LI SHEN

LMAM, School of Mathematical Sciences, Peking University
Beijing 100871, China

ERIC TODD QUINTO

Department of Mathematics, Tufts University
Medford, MA, U.S.A.

SHIQIANG WANG

College of Life Sciences, Peking University
Beijing 100871, China

MING JIANG*

LMAM, School of Mathematical Sciences,
Beijing International Center for Mathematical Research, Peking University
Beijing 100871, China
China Cooperative Medianet Innovation Center, Shanghai Jiao Tong University
Shanghai 200240, China

2010 *Mathematics Subject Classification*. Primary: 15A29, 47A52; Secondary: 68U10.

Key words and phrases. Image reconstruction, ill-posed problem, Mumford-Shah regularization, Electron tomography, Electron microscopy.

This work was partially supported by the National Basic Research Program of China (973 Program) (2015CB351803), National Research and Development Program of China (2016YFA0500401), the National Science Foundation of China (61520106004, 81370203, 81461148026), Sino-German Center (GZ 1025), U.S. National Science Foundation under grants (DMS1311558, DMS1712207 to E.T. Quinto), and Microsoft Research of Asia.

* Corresponding author: Ming Jiang.

ABSTRACT. Electron microscopy (EM) is a detection method for determining the structure of macromolecular complexes and biological specimens. However, some restrictions in the EM system, including poor signal-to-noise, limited range of tilt angles, only a sub-region subject to electron exposure and unintentional movements of the specimen, make the reconstruction procedure severely ill-posed. Because of these limitations, there may be severe artifacts in reconstructed images. In this paper, we first design an algorithm that can quickly calculate the radiological paths. Then we combine an iterative reconstruction algorithm using the Mumford-Shah model with an artifact reduction strategy. The combined method can not only regularize the ill-posedness and provide the reconstruction and segmentation simultaneously but also smooth additional artifacts due to the limited data. Also we improved the algorithm used for the calculation of radiological paths to accelerate the reconstruction. The proposed algorithm was translated into OpenCL programs and kernel functions to asynchronously and in parallel update the reconstructed image along rays by GPUs. We tested the method on both simulated and real EM data. The results show that our artifact reduced Mumford-Shah algorithm can reduce the noise and artifacts while preserving and enhancing the edges in the reconstructed image.

1. Introduction. Cryo-electron microscopy is a promising technique for imaging the high-resolution structure of macromolecular complexes. In the Transmission Electron Microscope (TEM) system, a small part of the specimen is illuminated by focused electrons. After the electron-specimen interaction, the electrons reach the detector and the intensity of electrons is recorded as grey-scale images (micrographs) [1]. Then the specimen is tilted in the beam and the projections are recorded from different directions. These projections are used to reconstruct the three-dimensional structure of the specimen [2]. The reconstruction problem in electron tomography (ET) is an example of a tomographic inverse problem.

There are some limitations in ET that do not appear in X-ray tomography that cause difficulties for the inverse problem in ET. The dose problem: The electron-specimen interaction may damage the structure of specimen, so the total dose of electrons during the detection must be limited. When a low-dose TEM is used, micrographs will have poor signal-to-noise ratio (SNR) with significant influence of shot noise [3]. The limited data problem: Only a small sub-region of the specimen can be illuminated by the electron beam and the tilt angles of specimen is restricted in a limited range. These limitations on the sub-region and range of the tilt angle lead to severe ill-posedness. Inversion algorithms using limited data can create artifacts, blurring, or other distortions in their reconstructions [4]. Reconstruction methods like the filtered back projection (FBP) algorithm in X-ray tomography require complete tomographic data. The FBP algorithm applied to limited data tomography will create additional artifacts in the reconstruction [5]. The alignment problem: there are accidental movements of specimen during the detection. Hence, correct alignment of micrographs before the reconstruction is necessary. Fiducial markers like gold beads are commonly used as accurate identifications to track the tilt angles and movements of the specimen [6].

Many simulation and reconstruction techniques have been introduced to ET. In [7], a simulation of transmission electron cryo-microscope images is applied to biological specimens with the mathematical model of electron-specimen and optical system in [8] [3]. Among the reconstruction methods, weighted back-projection (WBP) is the most widely used for its speed and simplicity of implementation [9].

In [10], conical tomography is used to study the structure of integral proteins and small volumes of the specimen are reconstructed by the WBP method. In [11], mice retinas were projected into conical tile series, reconstructed by WBP method, aligned by projection matching, and analyzed by semiautomatic density segmentation. However, the WBP method is easily affected by the limited data problem and poor (SNR) of projection data can create artifacts in reconstructed images. Electron lambda-tomography in [12] can preserve the simplicity and speed of WBP method but is less sensitive to the artifacts. Iterative methods such as the algebraic reconstruction techniques (ART) have a significant capability to provide greater detail with incomplete and noisy data [13]. In [2], WBP and ART reconstruction techniques from a series of tilted electron-tomographic projection images provide quantification of surface proteins on an influenza virus. It demonstrates that ART can provide 3D reconstructions of virus from tomographic tilt series that allow more reliable qualification of surface protein than the WBP method. Many regularization methods are applied to deal with the ill-posed problem, especially in cases of limited data. But a different choice of regularization methods can lead to different reconstruction results. Penalized least square approaches, such as Tikhonov and other regularization methods, were previously utilized in X-ray tomography. Recently, Mumford-Shah functionals have been studied for the simultaneous reconstruction and evaluation of images. In [14], the convergence of minimizers of a Mumford-Shah functional for the simultaneous reconstruction and segmentation of a distributed parameter in an ill-posed operator equation is demonstrated. In [4], the Mumford-Shah-like level-set approach is exploited to find a segmentation from limited data, and by that, the singularity set was found from simulated data of a two-dimensional torso phantom.

For most of the iterative reconstruction methods, the image is discretized into pixels and the line-integrals into weighted sums. These weighting factors are called radiological paths and are equal to the intersection length of the ray with each pixel. Because of the huge amount of measurements and the large number of pixels, it is impossible to store all radiological paths in a file prior to the reconstruction [15]. Hence, fast calculation of the radiological path for each specified ray is necessary to obtain acceptable reconstruction times [16]. In [17], the 3DDDA algorithm is one of the first algorithms that was used for the ray-tracing of a uniformly subdivided scene. In [16], one of the first algorithms is proposed that can provide exact and reliable radiological paths for three-dimensional CT. In [18], a code-based voxel-traversing algorithm is designed for voxel traversing based on the classic Bresenham line-drawing algorithm. The multi-step algorithm [19] improved the algorithm in [18] and reduced the time spent in the inner loop by using only integer operations. SNARK09 is a programming system designed to help researchers interested in developing and evaluating reconstruction algorithms [20]. It provides a fast iterative algorithm for the calculation of radiological path in 2D. We modified this algorithm from SNARK09 and extended it to the 3D case. This improved algorithm calculates the intersection length iteratively along the ray, and it needs only a few addition operations for most of the coefficients.

The Mumford-Shah functional has provided an important approach for image de-noising and segmentation. It has also been applied to image reconstruction in fields, such as X-ray tomography and electrical impedance tomography. The regularization terms in the Mumford-Shah functional not only force the smoothness of the images within individual regions but also simultaneously prevent smoothing

across image edges. Let Ω be a bound domain and $g \in L^\infty(\Omega)$ a noisy image. The variational approach in [21] is to find a pair (f, K) , where $K \in \Omega$ represents the edges in g and f is a smoothed approximation of g in $\Omega \setminus K$. In solving the inverse problems, the minimizing pair (f, K) can be understood as the a reconstruction and a segmentation from the projection data g . (f, K) is defined as a minimum of the functional

$$MS(f, K) := \int_{\Theta} |\mathcal{R}f - g|^2 dx + \alpha \int_{\Omega \setminus K} |\nabla f|^2 dx + \beta \text{length}(K), \quad (1)$$

where Θ is the set of all lines passing through Ω , \mathcal{R} is the *Radon transform*, $\alpha, \beta \in \mathbb{R}^+$. The three terms are: a least square squares term, forcing f to be the "real" reconstructed image from g ; a L^2 -penalty term for the gradient of f , forcing f to be smooth everywhere in Ω except at the edges K ; and a penalty of K 's length in 2D or area in 3D, forcing the edges K to be "short" or "small".

Our main goal in this article is to generalize the iterative algorithm with the Mumford-Shah model in [22] to the inverse problem in ET. To reduce the artifacts in ET, we combine the artifact reduction strategy in [5] with the reconstruction method. The Mumford-Shah model is both mathematically and computationally difficult, so we improve the algorithm used for the calculation of radiological paths to accelerate the reconstruction. Also the proposed algorithm is translated into OpenCL programs and kernel functions to asynchronously and in parallel update the reconstructed image by GPU devices.

The paper is organized as follows. Sec. 2 provides the mathematical model of ET and the strategy to reduce the artifacts caused by limited data. Sec. 3 introduces the proposed algorithm incorporating simultaneous image reconstruction and segmentation and describes our design methodology. Sec. 4 presents our main results. We present the reconstructions from simulated and real ET data to show the effects of the artifact reduction strategy and the iterative algorithm with a Mumford-Shah model.

2. Tomography. In this section, we provide a brief introduction to ill-posed problems and the mathematical models of the ET problem. Let X and Y be Hilbert spaces and $A : X \rightarrow Y$ a bounded linear operator. The *forward problem* is to compute (2) for a given function $f \in X$.

$$Af = g \quad (2)$$

The inversion of (2) is needed in the reconstruction procedure of X-ray tomography and electron tomography, i.e., to obtain the source f for a measurement $g \in Y$ under the operator A . If the operator A is linear and bounded, the reconstruction procedure is called a *linear inverse problem*. In this work, the operator A is the *Radon transform* in 3D,

$$\mathcal{R}f(\theta, y) = \int_{\mathbb{R}} f(t\theta + y) dt \quad (3)$$

where $\theta \in S^2$ with S^2 being the unit sphere in \mathbb{R}^3 and

$$y \in \theta^\perp := \{x \in \mathbb{R}^3 : x \cdot \theta = 0\},$$

the plane through the origin orthogonal to θ .

2.1. Mathematical Model of the Image Formation in Transmission Electron Microscopy. We briefly introduce the mathematical models of ET. In scattering theory [8] [3], the scattering potential that fully characterizes the scattering properties of the specimen is given as

$$F(x) := -\frac{2m}{\hbar^2}(V(x) + i\Lambda(x)) \quad (4)$$

where $V : \mathbb{R}^3 \rightarrow \mathbb{R}$ is the electrostatic potential and $\Lambda : \mathbb{R}^3 \rightarrow \mathbb{R}$ the inelastic potential. The real part of F , denoted as F^{re} , can be physically interpreted as the molecular structure of the specimen. The imaginary part F^{im} accounts for the decrease in the flux of the non-scattered and elastically scattered electrons. The purpose of ET is to reconstruct the three-dimension distribution of the F^{im} in the specimen.

Assume the imaging system is perfect, then the incident electron wave is a monochromatic plane wave (coherent illumination) u^{in} of the form

$$u^{in}(\omega, x) = e^{ikx \cdot \omega}, \quad (5)$$

where ω denotes the direction of propagation, k is the wave number of the plane wave. With the first-order Born approximation and elastic scattering assumption, the electron wave u^{obj} after the electron-specimen interaction can be derived from scalar Schrödinger as follows:

$$u^{obj}(\omega, y) = u^{in}(\omega, y) \left(\frac{i}{2k} \int_{-\infty}^r F(s\omega + y) ds \right) \quad (6)$$

where $y \in \omega^\perp$ is the immediate exit plane after the specimen.

After interacting with the specimen, the electron waves pass through the optical system of the electron microscope. The model for the optical system is based on the wave nature of imaging electrons and the scalar theory is used to characterise the diffraction of electron waves in light optic. The optical system can be roughly interpreted as the *objective lens*, *aperture* and the *projector lenses*. As the electron wave reaches the image plane, the intensity illuminated by a single electron is measured at the detector.

The *amplitude contrast model* in [3] adopts the *projection assumption* and give the expression for the intensity $I_k(F)$ generated by a single electron

$$\begin{aligned} I_k(F)(\omega, z) = & \frac{1}{M^2} (1 - (2\pi)^{-2} [\{\text{PSF}_k^{im}(\omega, \cdot) \underset{\omega^\perp}{\otimes} \mathcal{R}(F^{re})(\omega, -\cdot)\} \left(\frac{z}{M}\right) \\ & + \{\text{PSF}_k^{re}(\omega, \cdot) \underset{\omega^\perp}{\otimes} \mathcal{R}(F^{im})(\omega, -\cdot)\} \left(\frac{z}{M}\right)] k^{-1}) + O(k^{-2}) \end{aligned} \quad (7)$$

where $z \in \omega^\perp$ is the image plane. $\underset{\omega^\perp}{\otimes}$ denote the convolution operator on the two-dimensional plane ω^\perp . M is the magnification of the optical system and PSF is the *point spread function* that characterize the optical system. Assume that the ideal optics and ignore the aperture, i.e. $\text{PSF}_k^{im} \equiv 0$ and $\text{PSF}_k^{re}(\omega, \cdot) = \delta_{\omega^\perp}$ in (7), then the expression reads as

$$I_k(F)(\omega, z) \approx \frac{1}{M^2} \left(1 - (2\pi)^{-2} \mathcal{R}(F^{im}) \left(\omega, -\frac{z}{\omega} \right) k^{-1} \right) \quad (8)$$

Note that one can calculate the Radon transform of the imaginary part of the scattering potential F^{im} from the right-hand side of (8). Thus, it is reasonable to

modify the image reconstruction methods from X-ray tomography and apply them to the ET.

2.2. Limited data tomography. As we mentioned in the introduction, some restrictions in the EM system limit the application of ET in life sciences and result in the *limited data problem* explained below.

Irradiated by an electron beam, the specimen gets progressively damaged due to ionization. So the number of electrons used to irradiate the specimen needs to be low enough to preserve the structural integrity of the specimen. When the specimen tilts, electrons pass through longer distance in the specimen, and less electrons can reach the detector. Hence, the projections detected at high tilt angles have poor intensity contrast and tilt angles need to be in a limited range. Also in the TEM system, only a small part of the specimen is subject to electron exposure for one detection. The region of interest (ROI) is a subset of the intersected part of all exposed parts of the specimen from different positions. In the ET, ROI is a subset of the support of the scattering potential. We therefore deal with a *local* tomography problem. As a consequence, the scattering potential cannot be uniquely determined in spite of the quality or quantity of the detected data.

2.3. Reduction of artifacts in limited angle tomography. The reconstruction problem for *limited angle tomography* is that a portion of the projections $\mathcal{R}f$ at certain tilt angles is missing. The tilt angles we consider are those in

$$S_{\Phi}^2 := \{\theta \in S^2 : \theta = \pm(\sin \phi \cos \psi, \sin \phi \sin \psi, \cos \phi), |\phi| \leq \Phi, |\psi| \leq \pi/2\}, \quad (9)$$

and the *angular range parameter* Φ is assumed to satisfy $0 < \Phi < \pi/2$. For each $\theta \in S_{\Phi}^2$, the detector plane is the plane θ^{\perp} through the origin orthogonal to θ , and we denote the set over which data are taken by $T(S_{\Phi}^2)$ where, for $S \subset S^2$,

$$T(S) = \{(\theta, y) : \theta \in S, y \in \theta^{\perp}\}.$$

The single-axis tilt geometry can be described by Euler angles. It has azimuthal angle being 0° , in-plane rotation ψ fixed and rotation ϕ changing between a certain angle $\pm\Phi$. The angular range parameter is described by a subset of S_{Φ}^2 with fixed angle ψ_0 :

$$S_{\Phi, \psi_0}^2 := \{\theta \in S^2 : \theta = \pm(\sin \phi \cos \psi, \sin \phi \sin \psi, \cos \phi), |\phi| \leq \Phi, \psi = \psi_0\}.$$

To reconstruct images from the limited angle data, we denote the *limited angle Radon transform*

$$\mathcal{R}_{\Phi} : f \mapsto \mathcal{R}f|_{T(S_{\Phi}^2)} \quad (10)$$

and this transform takes data for $\theta \in S_{\Phi}^2$ instead of the data for all $\theta \in S^2$.

The back-projection (or dual operator) for the limited angle Radon transform is given by

$$\mathcal{R}n_{\Phi}^*g(x) = \int_{\theta \in S_{\Phi}^2} g(\theta, x - (x \cdot \theta)\theta) d\theta. \quad (11)$$

Note that $x - (x \cdot \theta)\theta$ is the orthogonal projection of x onto θ^{\perp} . For single axis tilt, the integral is over S_{Φ, ψ_0}^2 for the appropriate value of ψ_0 .

In X-ray CT there are usually streak artifacts at the end of the limited angular range in the reconstructed images. We briefly introduce the strategy we use to reduce these artifacts caused by limited angle, and readers can see [5] for details. We applied this artifact reduction strategy to the iterative reconstruction algorithm in

Sec. 3 although it was originally designed for the filtered back-projection (FBP) algorithm and Lambda tomography. This artifact reduction strategy is to apply more general weights on the target functional of reconstruction. Define the multiplication operator \mathcal{K}

$$\begin{aligned} \mathcal{K} : \mathcal{S}'(T(S^2)) &\rightarrow \mathcal{S}'(T(S^2)), \quad \mathcal{K}g(\theta, y) = \kappa(\theta)g(\theta, y) \\ \text{where } \kappa : S^2 &\rightarrow \mathbb{R}, \quad \text{supp}(\kappa) \subset S_{\Phi}^2 \end{aligned} \quad (12)$$

where κ is a smooth (i.e. C^∞) cutoff function $\kappa_\sigma : S^2 \rightarrow \mathbb{R}$. Then the multiplication operator

$$\mathcal{K}_\sigma g(\theta, y) = \kappa_\sigma(\theta)g(\theta, y) \quad (13)$$

Let $0 < \sigma < \Phi/2$ and define $\varphi_\sigma : [-\pi, \pi] \rightarrow [0, 1]$ to be a π -periodic function which is given by $\varphi_\sigma(x) = \exp(\frac{x^2}{x^2 - \sigma^2})$ for $|x| \leq \sigma$ and $\varphi_\sigma(x) = 0$ for $\sigma < |x| < \pi/2$. Then define the cutoff function $\kappa_\sigma : S^2 \rightarrow \mathbb{R}$ via

$$\kappa_\sigma(\theta(\phi)) = \begin{cases} \varphi_\sigma(\phi + (\Phi - \sigma)), & \phi \in [-\Phi, -(\Phi - \sigma)], \\ 1, & \phi \in [-(\Phi - \sigma), \Phi - \sigma], \\ \varphi_\sigma(\phi - (\Phi - \sigma)), & \phi \in [\Phi - \sigma, \Phi], \\ 0, & \text{else,} \end{cases} \quad (14)$$

where $\phi \in [-\pi, \pi]$. Note that $\kappa_\sigma \equiv 1$ on $S_{\Phi - \sigma}^2$ and has smooth transition from 1 to 0 in $S_{\Phi}^2 \setminus S_{\Phi - \sigma}^2$. There is a trade-off in choosing the parameter σ between the fidelity of reconstruction and the visibility of streaks. In our applications, we chose σ by experience.

In the next section, we will combine this artifact reduction strategy with a simultaneous reconstruction and segmentation method with the Mumford-Shah model and get an artifact reduced Mumford-Shah algorithm. The resulting reconstructions for $\sigma = \Phi/4$ are show in Fig.3. Here, we can clearly observe the effect of artifact reduction: While streak artifacts near $\pm 60^\circ$ in (c)+(d) and annular artifacts in (e)+(f) can be observed, the implementation of the artifact reduction strategy, using a cutoff κ_σ in the operator \mathcal{K}_σ , smooths some artifacts in (g)+(h) and (i)+(j).

3. Algorithm Description and Design Methodology. In this section we first introduce a fast iterative algorithm for calculation of radiological paths. Then we introduce the Mumford-Shah approach and an alternative minimization algorithm for the inverse problem in ET. Combine this algorithm with the artifact reduction strategy we introduced before, we can get an artifact reduced Mumford-Shah algorithm. Finally we translate the proposed algorithm into OpenCL programs and kernel functions to asynchronously and in parallel update the reconstructed image along rays by GPUs.

3.1. Fast calculation of radiological paths. Most of the computational demand is from Radon transform \mathcal{R} and its adjoint operator \mathcal{R}^* . In limited angle tomography, it is \mathcal{R}_Φ and \mathcal{R}_Φ^* defined in (10)(11). The discretized form of \mathcal{R} and \mathcal{R}^* can be expressed as

$$g_i = \sum_j l_{ij} f_j, \text{ and } f_j = \sum_i l_{ij} g_i \quad (15)$$

where f_j is the j -th pixel (or voxel in 3-dimensional) of the linearized image $f_{1\dots J}$, g_i is the i -th component of the measured attenuation rates $g_{i\dots I}$, and l_{ij} is the

contribution coefficient of the j -th pixel to the attenuation of the i -th measured line. The coefficient l_{ij} equals to the intersection length of the ray with pixel (i, j) [17]. Therefore, the computation of projection and back-projection can be reduced to the generation of radiological paths l_{ij} .

Because of the huge amount of measurements in electron tomography and the large number of pixels or voxels, it is impossible to store all weighting factors l_{ij} prior to the reconstruction. Hence, the l_{ij} need to be calculated on the fly, which cost most of the computation demand. A fast algorithm to calculate radiological paths is a necessity to obtain acceptable reconstruction times. Currently, one of the fastest algorithms designed for this purpose in 2D is the ray-trace algorithm is SNARK09 programming system [20]. We improved this algorithm in a way that the time spent in the inner loop is reduced considerably (also see [23]) and extended it to rays lying in 3D.

The basic idea of the algorithm is to compute $l_{i,2}, l_{i,3}, \dots, l_{i,J}$ along a ray iteratively when given $l_{i,1}$. In such a way, only addition operations are needed for most of the coefficients, instead of the time-consuming trigonometric functions. The procedure calculates the index (ia, ib) of the first intersection pixel and the intersection length array **length**. Because the slope of the ray is a constant, the index of the next pixel intersected by the same ray can be determined according to the current intercepts, and the lengths of the ray segments can also be derived from intercepts by dividing one of the intercepts with the slope. For every iteration, it calculates the lengths of the ray segments within the current pixel, determine the index of the next pixel intersected, then calculate the ray intercepts on the next pixel by adding or subtracting a constant on the current intercepts.

Assume a ray through the reconstruction area is perpendicular to a vector ω , let φ be the angle between the ray and x -axis, then $\varphi = \arg(\omega^\perp)$. Then our algorithm used for the calculation of radiological paths in 2D is briefly shown in Algorithm. 1.

```

input ray in 2D;
Initialize  $w, ia, ib$ ;
while  $((ia, ib)$  in image) do
  if  $w < 1$  then
     $w = w + \cot(\varphi) - 1$ ;
    length $[ia, ib] = w * L$ ;
    length $[ia, ib + 1] = L - \mathbf{length}[ia, ib]$ ;
     $ib = ib + 1$ ;
  end
  else
     $w = w - 1$ ;
    length $[ia, ib] = L$ ;
  end
   $ia = ia + 1$ ;
end

```

Algorithm 1: Fast calculation of 2D radiological paths

In Algorithm. 1, the variable φ is the angle of inclination and (ia, ib) is the index of the pixel. As shown in Fig. 1. The variable L is the intersection length

of a ray with two vertical gridlines and w is the proportion between intersection length of current pixel and L . The calculation of latitude of $\mathbf{length}[ia + 1, ib]$ and $\mathbf{length}[ia, ib + 1]$ depend on the calculation of $\mathbf{length}[ia, ib]$.

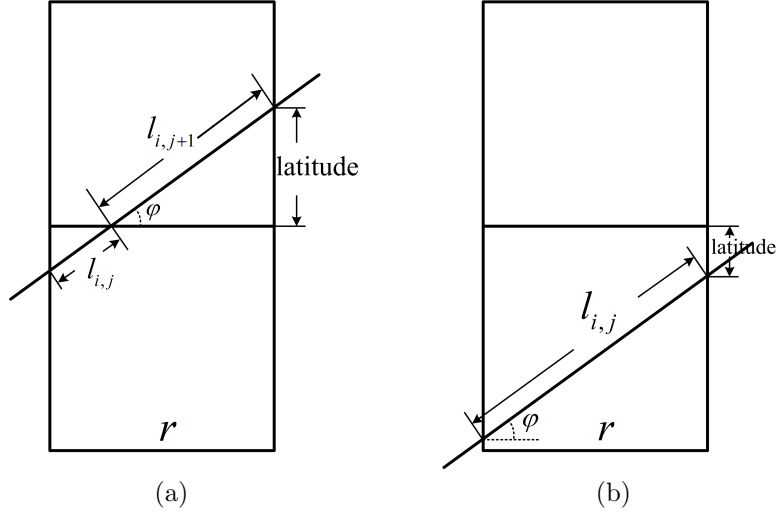


FIGURE 1. Illustration of the calculation of 2d radiological paths. The variable φ is the angle of inclination and (ia, ib) is the index of the pixel. The variable L is the intersection length of a ray with two vertical gridlines and w is the proportion between intersection length of current pixel and L . The current pixel intercepted by the ray is (ia, ib) . $w > 1$ in Algorithm. 1 corresponds to the left figure where the next pixel intercepted by the ray is $(ia, ib + 1)$ and $w < 1$ corresponds to the right figure where the next pixel is $(ia, ib + 1)$. The proportion w is calculated alternatively in Algorithm. 1 including only a few addition or subtraction operations and w is used to decide whether the next pixel intercepted by the ray corresponds to the case in the left figure or the right figure.

Except for one time of multiplication $w * L$ in each loop, the calculation of the ray intercepts on the next pixel only include a few addition or subtraction operations on the current proportion w of current intercepts. At each loop of the algorithm, the index ia always increases by 1, so the so the maximum time of the iteration is the number of elements along the larger dimension of the 2D reconstruction grid.

We extend Algorithm. 1 for the calculation of radiological paths in 3D case. Assume a ray in 3D space has the z -axis as a principal axis (the angle between the ray and z -axis is smaller than that between other axes). Assume the current calculation voxel is (ia, ib, ic) , then we calculate along the z -axis; i.e., decide which voxel the ray will pass through and the intersection length with each voxel when the index ic in z -axis direction increase by 1.

First, we project the ray into zx -plane and zy -plane respectively and turn the 3D radiological path calculation problem into two calculations of 2D radiological paths for which we already have a solution. Second, we use the Algorithm. 1 to calculate the proportion w_x of the projected ray in zx -plane and w_y in zy -plane. Finally, the process in Algorithm. 2 is used to decide the voxel and calculate the

intersection length. In algorithm. 2, w_x and w_y are the proportion of the projected

```

input  $w_x, w_y$ ;
while  $((ia, ib, ic)$  in image) do
     $w_x = \min(w_x, 1)$ ;
     $w_y = \min(w_y, 1)$ ;
    if  $w_x < w_y$  then
        length $[ia, ib, ic] = w_x * L'$ ;
        length $[ia + 1, ib, ic] = (w_y - w_x) * L'$ ;
        length $[ia + 1, ib + 1, ic] = L' - w_y * L'$ ;
    end
    else
        length $[ia, ib, ic] = w_y * L'$ ;
        length $[ia, ib + 1, ic] = (w_x - w_y) * L'$ ;
        length $[ia + 1, ib + 1, ic] = L' - w_x * L'$ ;
    end
     $ic = ic + 1$ ;
end

```

Algorithm 2: Fast calculation of 3D radiological paths

ray in zx - plane and zy - plane respectively shown in Fig. 2. w_x and w_y are calculated by algorithm. 1. L' is the constant length of the ray between the plane $iz = ic$ and $iz = ic + 1$. As shown in Fig. 2, the current voxel intercepted by the ray is (ia, ib, ic) . $w_x < w_y$ in Algorithm. 2 corresponds to case that the next two voxels intercepted by the ray are $(ia + 1, ib, ic)$ and $(ia + 1, ib + 1, ic)$. $w_x \geq w_y$ corresponds to case that the next two voxels are $(ia, ib + 1, ic)$ and $(ia + 1, ib + 1, ic)$. w_x and w_y are used to decide which voxels are intercepted by the ray after the current voxel (ia, ib, ic) . Note that when $w_y = 1$, **length** $[ia + 1, ib + 1, ic] = 0$ and voxel $(ia + 1, ib + 1, ic)$ is not intersected by the ray. The calculation of radiological paths of a ray in 3D space is just a combination of Algorithm. 1 and Algorithm. 2. Also in the 3D case, the ic increase by 1 at each loop, so the maximum time of the iteration is also the number of elements along the largest dimension of the 3D reconstruction grid.

3.2. The Mumford-Shah approach. The forward process maps an image into the set of its line integrals. The mathematical model for X-raying an object is the *Radon transform* \mathcal{R} defined in (3). Suppose $g = \mathcal{R}f^\dagger$ as the measured projection data of the true density f^\dagger of the object. To find an image f such that $\mathcal{R}f = g$ is the purpose of solving the inverse problem. In ET, f^\dagger is referred to as the imaginary part F^{im} of scattering potential in (8).

A simultaneous reconstruction and segmentation can be formulated as finding an image f and a meaningful decomposition

$$\Omega = R_1 \cup R_2 \cup \dots \cup R_l \cup K \quad (16)$$

of the image domain Ω , where $R_i \subset \Omega$ are disjoint connected open subsets, K is the union of the boundaries of R_i in Ω . The image f is an approximation to the true image f^\dagger such that

- f varies smoothly and/or slowly within each R_i , and

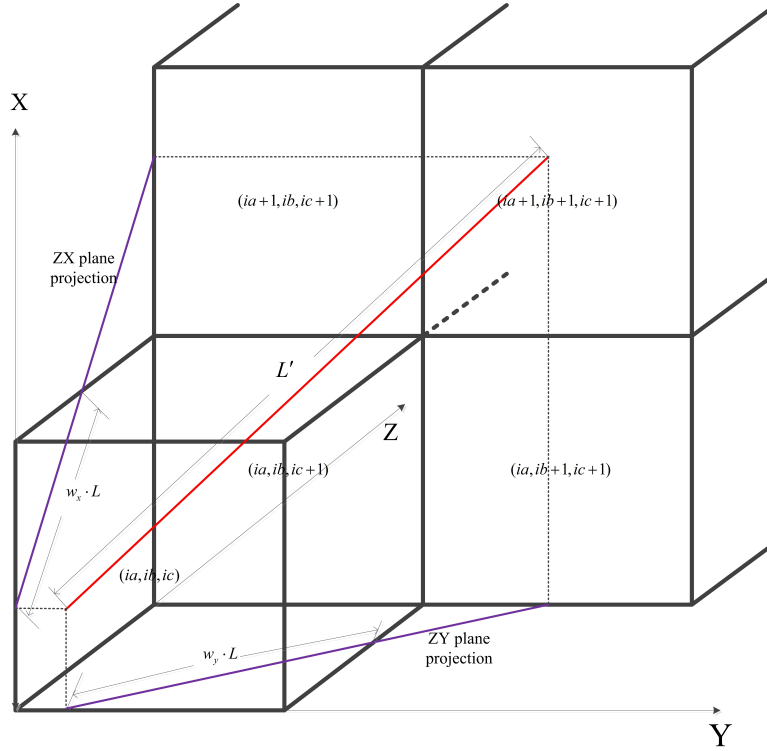


FIGURE 2. Illustration of the calculation of 3d radiological paths. w_x and w_y are the proportion of the projected ray in zx -plane and zy -plane respectively. w_x and w_y are calculated by algorithm. 1. L' is the constant length of the ray between the plane $iz = ic$ and $iz = ic + 1$. The current voxel intercepted by the ray is (ia, ib, ic) . $w_x < w_y$ in Algorithm. 2 corresponds to case that the next two voxels intercepted by the ray are $(ia + 1, ib, ic)$ and $(ia + 1, ib + 1, ic)$. $w_x \geq w_y$ corresponds to case that the next two voxels are $(ia, ib + 1, ic)$ and $(ia + 1, ib + 1, ic)$. w_x and w_y are used to decide which voxels are intercepted by the ray after the current voxel (ia, ib, ic) .

- f varies discontinuously and/or rapidly across K

In this work, we focus on the pair (f, K) in 3D. We minimize the following Mumford-Shah type functional to obtain (f, K) [21]

$$MS(f, K) := \int_{\Theta} |\mathcal{R}f - g|^2 d\theta ds + \alpha \int_{\Omega \setminus K} |\nabla f|^2 dx + \beta \text{area}(K), \quad (17)$$

where $\Omega \subset \mathbb{R}^3$ is the image domain, $\Theta \subset T(S^2)$ parameterizes the set of all lines passing through Ω , $f \in \Omega$ is a piecewise smooth image, $K \in \Omega$ are the edges, and $\alpha, \beta \in \mathbb{R}^+$. The integration variables in the first term are $\theta \in S^2$ and $s \in \mathbb{R}^2$. Here $\nabla f = (\frac{\partial f}{\partial x}, \frac{\partial f}{\partial y}, \frac{\partial f}{\partial z})$ is the gradient of f . The objective functional $MS(f, K)$ contains

three terms: a least squares term that force f to match the measured projection g ; a L^2 -penalty term for the ∇f that force f to be smooth everywhere in Ω except at the edges K ; and a penalty of K 's area that force the edges K to be "small".

Several issues arise when applying the Mumford-Shah regularization to practical applications. The primary difficulty is how to represent the edge set K in computer code and to trace its updates. We follow the approach in [24], where the edges are approximated by smooth edge indicator functions and the Mumford-Shah penalty is modified with Γ -approximation. We minimize the functional

$$\begin{aligned} AT_\varepsilon(f, v) &= \int_{\Theta} |\mathcal{R}(f) - g|^2 d\theta ds + \alpha \int_{\Omega} v^2 |\nabla f|^2 dx \\ &+ \beta \int_{\Omega} \left(\varepsilon |\nabla v|^2 + \frac{(1-v)^2}{4\varepsilon} \right) dx, \end{aligned} \quad (18)$$

for a small constant $\varepsilon > 0$.

Here, f is still the image. v is an image, defined on the interval $[0,1]$, and indicates the edge set K . The heuristic idea is that if $v \approx 0$ the gradient of f is only penalized a little but the last term is big. If $v \approx 1$ the last term nearly vanishes but the gradient of f is fully taken into account. Therefore $v \approx 0$ represent the presence and $v \approx 1$ the absence of an edge. The pair (f, v) is a solution to the simultaneous reconstruction and segmentation problem.

The convergence of the approximation in (18) to the original Mumford-Shah formulation in (17) in terms of Γ -convergence as $\varepsilon \rightarrow 0$ has been established when \mathcal{R} is the identity operator in [24] and when \mathcal{R} is more general forward operators, including the Radon transform, in [22]. Hence, a minimizer AT_ε is an approximated minimizer of $MS(f, K)$ when $\varepsilon \rightarrow 0$.

In order to combine AT_ε in (18) with artifact reduction strategy in section 2.3, we modify the AT_ε into $AT_{\varepsilon, \sigma}$ defined in (19).

$$\begin{aligned} AT_{\varepsilon, \sigma}(f, v) &= \int_{\Theta} |\mathcal{K}_\sigma(\mathcal{R}_\Phi(f) - g)|^2 d\theta dy + \alpha \int_{\Omega} v^2 |\nabla f|^2 dx \\ &+ \beta \int_{\Omega} \left(\varepsilon |\nabla v|^2 + \frac{(1-v)^2}{4\varepsilon} \right) dx, \end{aligned} \quad (19)$$

where the \mathcal{R}_Φ is limited angle Radon transform defined in (9), and the cutoff operator \mathcal{K}_σ defined in (13) is applied to both the Radon transform of f and the projection data g . A minimizer of the modified Mumford-Shah functional can be a solution with resistance to the streak artifacts caused by the limited angle problem. For the minimization of the Mumford-Shah functional we briefly describe the following algorithm from [22].

Our model in (18) derived from Ambrosio-Tortorelli approach in [24] seems quite similar to Modica-Mortola phase transition model [25] because both can be formulated with the Mumford-Shah functional and computed by its Γ -approximations. Both Γ -approximations of Modica-Mortola and Ambrosio-Tortorelli provide two practical approaches for image segmentation. However, there are two major differences:

- From the general perspective of pattern recognition, image segmentation is a clustering problem. One fundamental and difficult issue in this regard is if the number of clusters or classes is known before hand [26] [27]. The methods in

the [28] and [29] assume that the number of segmentations, i.e., the number N of phase levels, is *a priori* known. The Multiphase-field formulation in [29] also requires the number N of phase levels to be known in advance. On the other hand, the Γ -approximation of the edge term in our paper does not require the number of segmentations known *a priori*.

- Although the double-well term $v^2(1-v)^2/\varepsilon$ in Modica-Mortola model and one part $(1-v)^2/\varepsilon$ in (18) look similar, they are proposed for different purposes. The double-well term is used for modeling two mixtures components and has to be modified for multiphase-field [29]. The term $(1-v)^2/\varepsilon$ in (18) is selected from a family of Γ -approximations by Ambrosio-Tortorelli results, simply because it is easy for computation.

When the number of segmentations is known beforehand, the Modica-Mortola version should be applied. Otherwise, the Ambrosio-Tortorelli version is recommended.

3.3. Iterative algorithm. We introduce an alternating minimization scheme described in Algorithm 3 to compute a minimizer of $AT_{\varepsilon,\sigma}(f, v)$. Algorithm 3 is a block coordinate gradient descent (CGD) instance alternatively for f and v . In the first subroutine we keep the edge variable v fixed and minimize $AT_{\varepsilon,\sigma}(f, v)$ in f , then f is fixed and v is minimized in the second subroutine. This procedure is repeated for a number of iterations and a minimizer of $AT_{\varepsilon,\sigma}(f, v)$ can be found.

Initial values can be chosen as the zero image and no edges inside the image, i.e. the edge-set is set to 1. In our applications, the initial image is the reconstructed image from WBP method to reduce the iteration time.

The functional $AT_{\varepsilon,\sigma}(f, v)$ is convex in f and v separately although it is not jointly convex. Therefore, in each of the subroutines, we use an iterative gradient descent methods of the form

$$\phi^{i+1} = \phi^i + c_i d^i, \quad (20)$$

where ϕ is either f or v , depending on which variable we are minimising in the subroutine, d is an appropriate descent direction and c is the step size. Either the variation $\nabla_f AT_{\varepsilon,\sigma}$ or $\nabla_v AT_{\varepsilon,\sigma}$ is the descent direction d in a subroutine.

The variations of AT_{ε} with respect to (f, v) are

$$\nabla_f AT_{\varepsilon,\sigma}(f, v) = 2\mathcal{R}_{\Phi}^*(\mathcal{K}_{\sigma}(\mathcal{R}_{\Phi}(f) - g)) - 2\alpha \operatorname{div}(v^2 \nabla f), \quad (21)$$

$$\nabla_v AT_{\varepsilon,\sigma}(f, v) = 2\alpha |\nabla f|^2 v + \frac{\beta}{2\varepsilon}(v-1) - 2\beta\varepsilon \Delta v, \quad (22)$$

where \mathcal{R}_{Φ}^* is the adjoint operator of the limited angle Radon transform defined in (11), $\Delta v = \frac{\partial^2 v}{\partial x^2} + \frac{\partial^2 v}{\partial y^2} + \frac{\partial^2 v}{\partial z^2}$ and $\operatorname{div}(F) = \frac{\partial F_x}{\partial x} + \frac{\partial F_y}{\partial y} + \frac{\partial F_z}{\partial z}$, for $F = (F_x, F_y, F_z)$.

The Algorithm 3 used to minimize $AT_{\varepsilon,\sigma}(f, v)$ is composed of two subroutines. The first subroutine shown in Algorithm 4 minimizes $AT_{\varepsilon,\sigma}(f, v)$ in the image variable. The second subroutine shown in Algorithm 5 minimizes $AT_{\varepsilon,\sigma}(f, v)$ in the edge variable. We use the projected steepest descent method in both subroutines.

There are a number of convergence results for the general coordinate descent (CD) method for convex objective functions, but one cannot expect a general convergence result for a non-convex case [27] [30]. For non-convex objective functions, the work of [27] [31] shows that inexact search (i.e., finding inexact minimum in each coordinate descent step) does not only guarantee the convergence for non-convex functions, but also can help resolve the failure of CD method with exact search for Powell's counterexample. Because our final objective functional in (18) is not

```

 $f^0 = 0$  or a-priori image;
 $v^0 = 1$ ;
for  $i = 0$  to  $Iterations_{Alt} - 1$  do
   $\mathbf{f}^{i+1} = \arg \min_f (AT_{\varepsilon, \sigma}(\mathbf{f}, \mathbf{v}^i))$  with  $\mathbf{f}^i$  as initial value;
   $\mathbf{v}^{i+1} = \arg \min_v (AT_{\varepsilon, \sigma}(\mathbf{f}^{i+1}, \mathbf{v}))$  with  $\mathbf{v}^i$  as initial value;
end

```

Algorithm 3: Alternate Minimization of $AT_{\mathcal{R}, \varepsilon}(\mathbf{f}, \mathbf{v})$

```

 $\mathbf{f}^0 =$  current image;
 $\mathbf{v} =$  current edge;
 $\mathbf{d}^0 = \mathcal{R}^*(\mathcal{K}_\sigma(\mathbf{g}) - \mathcal{R}_\Phi(\mathbf{f}^0)) + \alpha \operatorname{div}(\mathbf{v}^2 \nabla \mathbf{f}^0)$  ;
 $\mathbf{p}^1 = \mathbf{d}^0$ ;
for  $i = 1$  to  $Iterations_{image} - 1$  do
   $c_1^i = \langle \mathbf{p}^i, \mathbf{d}^{i-1} \rangle_{L^2} / (\|\mathcal{R}_\Phi(\mathbf{p}^i)\|_{L^2}^2 + \|\mathbf{v}^2 \nabla \mathbf{p}^i\|_{L^2}^2)$ ;
   $\mathbf{f}^i = \mathbf{f}^{i-1} + c_1^i \mathbf{d}^i$ ;
   $\mathbf{d}^i = \mathcal{R}_\Phi^*(\mathcal{K}_\sigma(\mathbf{g}) - \mathcal{R}_\Phi(\mathbf{f}^i)) + \alpha \operatorname{div}(\mathbf{v}^2 \nabla \mathbf{f}^i)$  ;
   $\mathbf{p}^{i+1} = \mathbf{d}^i$ ;
end

```

Algorithm 4: Image Minimization with Steepest Descent Method

```

 $\mathbf{f} =$  current image;
 $\mathbf{v}^0 =$  current edge;
for  $i = 0$  to  $Iterations_{edge} - 1$  do
   $\mathbf{d}^i = -\alpha |\nabla \mathbf{f}|^2 \mathbf{v}^i - \frac{\beta}{4\varepsilon} (\mathbf{v}^i - 1) + \beta \varepsilon \Delta \mathbf{v}^i$  ;
   $c^i = \|\mathbf{d}^i\|_{L^2}^2 / (\alpha \|\nabla \mathbf{f}\|^2 \|\mathbf{d}^i\|_{L^2} + \beta \varepsilon \|\nabla \mathbf{d}^i\|_{L^2}^2 + \frac{\beta}{4\varepsilon} \|\mathbf{d}^i\|_{L^2}^2)$ ;
   $\mathbf{v}^{i+1} = \mathbf{v}^i + c^i \mathbf{d}^i$ ;
   $\mathbf{v}^{i+1} = \max(0, \min(1, \mathbf{v}^{i+1}))$ ;
end

```

Algorithm 5: Edge Minimization with Steepest Descent Method

jointly convex in f and v , we choose an inexact gradient descent approach rather than solving each step using closed form solution.

Although the coordinate descent algorithm with inexact search in [27] [31] converges, it still uses a line search along the descent direction in each step, i.e., the Armijo line search, to ensure sufficient decrease at each step. However, such a line search is impractical for large scale problems such as our case [27].

Another reason for us to choose the current the CGD algorithm is because our next implementation is with FPGA, despite there is no convergence results when the objective functional is non-convex. The current steepest descent is not only used to demonstrate the feasibility of a Mumford-Shah functional for limited angle tomography, but also is an economical choice for our later FPGA implementation in terms of algorithmic complexity, onboard memory and communication costs. A closed form solution for the v -step seems attractive, but it needs more memory and will increase communication cost from FPGA to CPU/RAM. We have encountered the same issue for our other imaging applications, where problems of the same image size can be solved with closed form in the Fourier domain.

3.4. OpenCL implementation. In order to accelerate the artifact reduced Mumford-Shah algorithm proposed in Sec. 2.3, we translated the algorithm into OpenCL programs and kernel functions that the GPUs will execute.

In OpenCL, a program is executed on a *computational device*, which can be a CPU, GPU, or another accelerator [32]. OpenCL’s key programming includes the steps below. First, create a *context* bundled with one or more devices. Second, transmit the source code into OpenCL compilation functions and obtain handles for the *kernel* functions. Finally, the kernels can then be launched on devices within the Open CL context. OpenCL host-device memory I/O operations and kernels are executed by enqueueing them into one of the command queues associated with the target device.

For the artifact reduced Mumford-Shah algorithm, the image minimization and edge minimization can be implied along each ray. Loop the rays in Radon transformation and calculate the steepest descent and update the data in reconstructed image or edge set along a ray.

We accelerate the algorithm by replacing this loop of rays with the OpenCL dispatcher. Then the OpenCL kernel becomes the calculation of steepest descent and the update of data in reconstructed image along a ray. We set the OpenCL global work-group size to the total number of rays i.e., *number of detectors* \times *number of angles*. Each work-item that OpenCL dispatches is responsible for the calculation and update along several rays using the kernel. Each OpenCL work-item determines its ray indexes from its global work-item index. Thus, the reconstructed image and edge are updated asynchronously and in parallel.

The strategy to select rays in each OpenCL work-item determine the order of rays picked for the reconstruction. In our applications, we chose one ray of each four rays along the detector axis in one projection as a work-item. Thus the rays in one work-item is far enough from each other and can not intersect the same voxel. The dispatcher in work-item is data-parallel and can be computed independently. Although there are output conflicts among different work-groups, it does not affect the reconstruction procedure in our applications. With our strategy for the OpenCL dispatcher, the global work-group size is the total number of rays, the local work-group size can be some multiple of the hardware *single-instruction multiple-data* (SIMD) [33] width as the maximum.

4. Applications. In this section, we test the artifact reduced Mumford-Shah algorithm in three examples. For the first example we test the results of the artifact reduction strategy in Sec 2.3. For the second example, we reconstruct the images and segmentations from noisy simulated data. In the last example, the algorithm is applied to cryo-electron tomography.

4.1. Reconstructions with the alternating minimization algorithm and artifact reduction strategy. We reconstructed the 3D Shepp-Logan phantom using the artifact reduced Mumford-Shah algorithm described in Algorithm 3 and compared the effects of the artifact reduction strategy in Sec. 2.3. Slices of the original phantom, reconstructed image and segmentations are shown in Fig.3. The tilt angular range is $-60^\circ \sim 60^\circ$ and the size of Shepp-Logan phantom is $300 \times 300 \times 300$. Fig.3(a)(b) are slices of original phantom. (a) corresponds to the red line in (b) and (b) to the red line in (a). Euler angles is used to generate projections: rotation ϕ changes between -60° and 60° at 1° intervals for each measurement, azimuthal angle θ is fixed at 0° and in-plane rotation ψ at 165° . (c)+(d) and (e)+(f) show

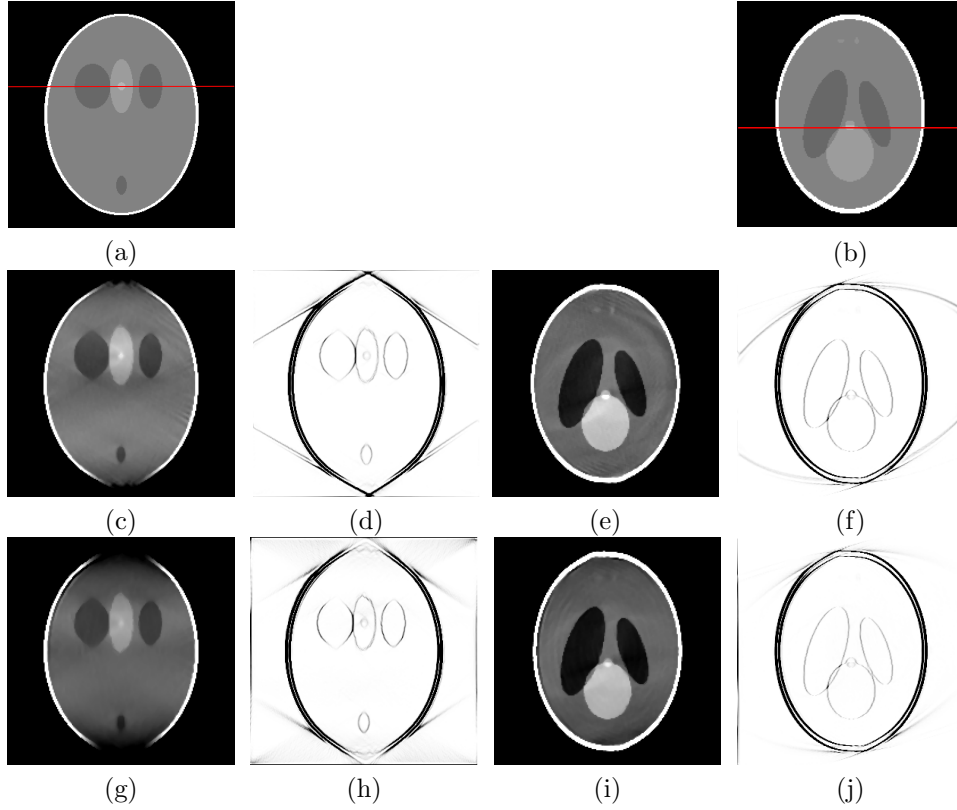


FIGURE 3. Reconstructions of 3D Shepp-Logan phantom using the alternating minimization scheme described in Algorithm 3 and artifact reduction strategy in Sec. 2.3. The size of Shepp-Logan phantom is $300 \times 300 \times 300$ and two slices are shown in (a) (e). (a)(b) are slices of original phantom. (a) corresponds to the red line in (b) and (b) to the red line in (a). Euler angles are used to generate projections: rotation ϕ changes between -60° and 60° at 1° intervals for each measurement, azimuthal angle θ is fixed at 0° and in-plane rotation ψ at 165° . (c)+(d) and (e)+(f) show the reconstruction image and segmentations without the artifact reduction strategy and (g)+(h) and (i)+(j), with a cutoff κ_σ in the operator \mathcal{K}_σ defined in (14). We chose the parameter $\sigma = \Phi/4$. While streak artifacts near $\pm 60^\circ$ in (c)+(d) and streak artifacts in (e)+(f) can be observed, the implementation of the artifact reduction strategy smooths some artifacts in (g)+(h) and (i)+(j).

the reconstruction image and segmentations without the artifact reduction strategy and (g)+(h) and (i)+(j), with a cutoff κ_σ in the operator \mathcal{K}_σ defined in (14). We chose the parameter $\sigma = \Phi/4$. While streak artifacts near $\pm 60^\circ$ in (c)+(d) and also streak artifacts in (e)+(f) can be observed, the implementation of the artifact reduction strategy smooth some artifacts in (g)+(h) and (i)+(j).

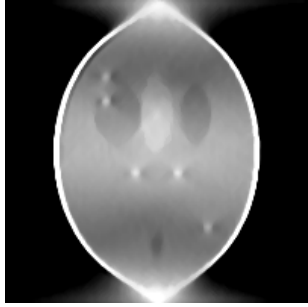
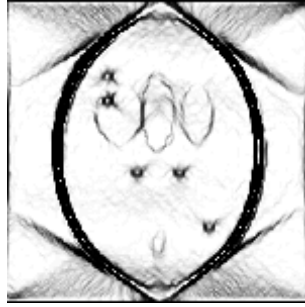
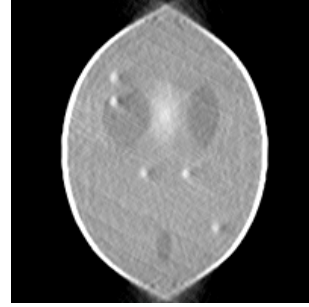
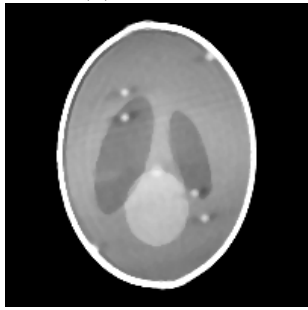
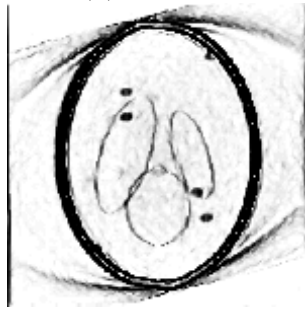
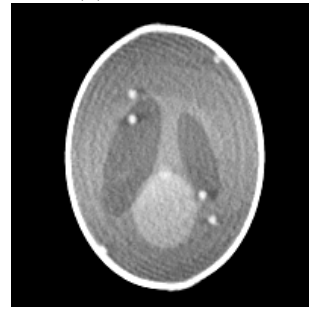
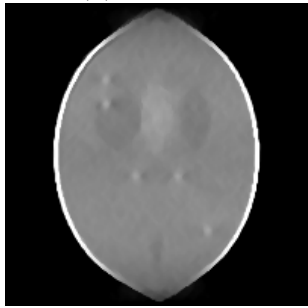
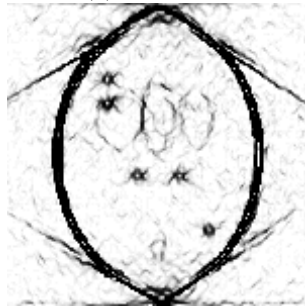
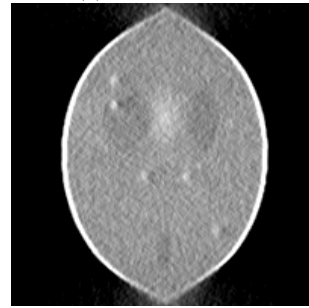
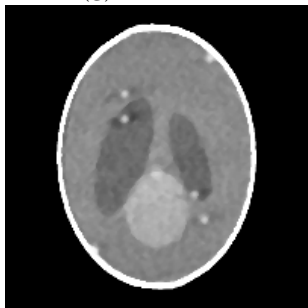
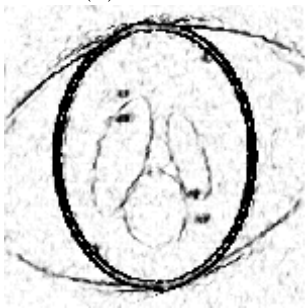
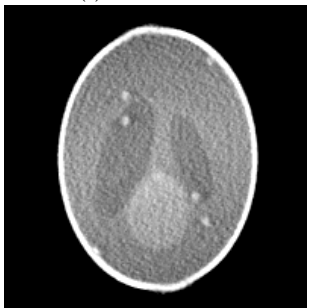
4.2. Reconstructions from the simulated data. The artifact reduced Mumford-Shah algorithm is applied to simulated ET data. The projection data is from noisy data $\mathcal{R}f^\dagger + \delta N(0, 1)$, where f^\dagger represents the $300 \times 300 \times 300$ Shepp-Logan phantom and $N(0, 1)$ represents standard normal distribution. The reconstructions are displayed for $\delta = 1, 2, 3, 4, 5$. The rotating axis and tilt angles is same as that in Sec.4.1: rotation ϕ changes between -60° and 60° at 1° intervals for each measurement, azimuthal angle θ is fixed at 0° and in-plane rotation ψ at 165° .

In order to simulate the alignment in ET, we inserted several golden particles in the phantom and add position disturbances on the projection data. The alignment of projection data was done by TOM software toolbox [6]. After alignment, we reconstructed separately with our artifact reduced Mumford-Shah algorithm and WBP method in TOM software toolbox. Reconstruction results are shown in Fig.4. For stronger noise, it is more difficult to reconstruct the low contrast regions for both methods. From the comparison between the left and right column, we can see that our reconstruction method with Mumford -Shah functional can depress the noise compared to WBP method while the edges are preserved. If an edge is detected in v , the reconstruction f^{MS} has a sharp edge.

4.3. Applications on Cryo-electron tomography. We applied both our method and WBP method to the cryo-electron tomography. Animals were approved by the Institutional Animal Care and Use Committee of Peking University (accredited by Association for Assessment and Accreditation of Laboratory Animal Care International). Single ventricular myocytes were enzymatically isolated from the hearts of adult male Sprague-Dawley rats (200-250 g) [34] [35]. We use a FEI tecani 20 TEM and single-axis tilt geometry to detect the cryo-specimen. Measurements are equally spaced between $-60^\circ \sim 60^\circ$ at 1° intervals for 121 angles. We adopt the TOM toolbox in [6] to align the projection data and use the WBP method in it to reconstruct the structure. Two slices of the reconstructed results are shown in Fig.5. The images in the red block are zoomed in and put in the top right corner. Compared to the reconstructions with WBP method, the noise and artifacts in our reconstructions are reduced with our method while the edges are preserved and enhanced.

We adopted the method in [36] to analyze the resolution of cryo-specimen reconstruction. The resolution maps are shown in Fig.6. The input map has the voxel size of 4.60\AA . The density maps and resolution maps are shown in Fig.6. The mean resolution of the reconstructed images with WBP method is 17.17\AA while the mean resolution of the artifact reduced Mumford-Shah algorithm is 15.07\AA .

5. Conclusion. We have combined the artifact reduction strategy in [5] and the reconstruction algorithm with the Mumford-Shah functional in [22]. The application of this method on both simulated data and cryo-specimen data shows that, for ET data, this reconstruction method can reduce the noise and artifacts caused by limited data problem while the edges in the reconstructed image is preserved and enhanced.

(a) MS $\delta = 1$ (b) MS $\delta = 1$ (c) WBP $\delta = 1$ (d) MS $\delta = 1$ (e) MS $\delta = 1$ (f) WBP $\delta = 1$ (g) MS $\delta = 3$ (h) MS $\delta = 3$ (i) WBP $\delta = 3$ (j) MS $\delta = 3$ (k) MS $\delta = 3$ (l) WBP $\delta = 3$

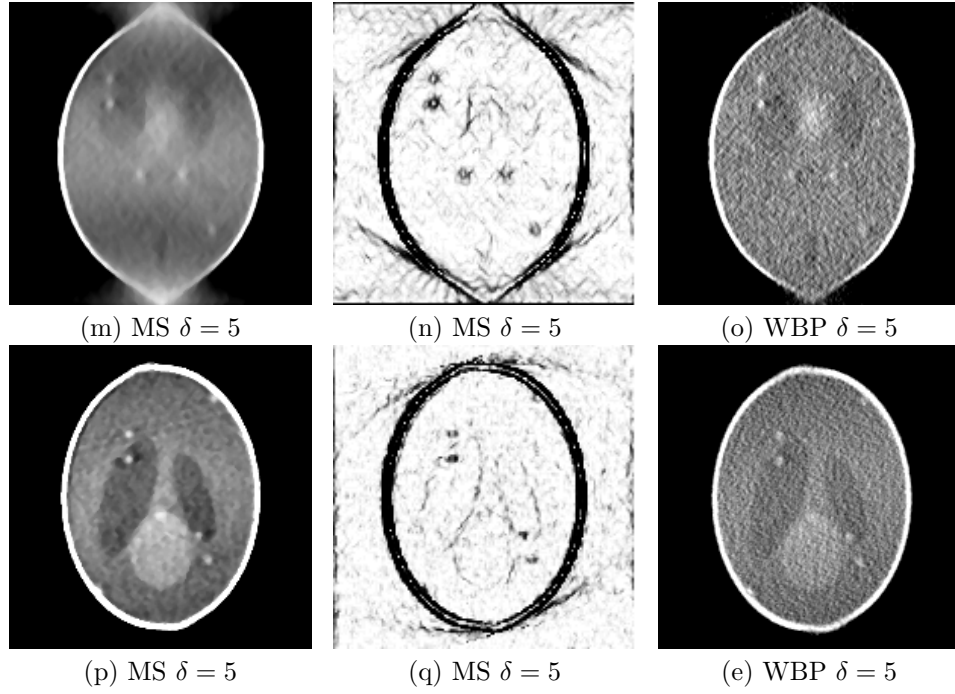


FIGURE 4. Reconstructions and segmentations of the Shepp-Logan phantom f^\dagger from noisy Radon data. Left column: reconstruction f^{MS} from noisy data $\mathcal{R}f^\dagger + \delta N(0, 1)$ using the artifact reduced Mumford-Shah algorithm ($\alpha = 2, \beta = 0.0002, \varepsilon = 0.0001$); middle column: The reconstructed edge indicator function v ; right column: reconstructions from same noisy data using WBP method in TOM software toolbox. For stronger noise it is more difficult to reconstruct the low contrast regions for both methods. From the comparison between the left and right column, we can see that our reconstruction method with Mumford-Shah functional can depress the noise compared to WBP method while the edges are preserved. If an edge is detected in v , the reconstruction f^{MS} has a sharp edge.

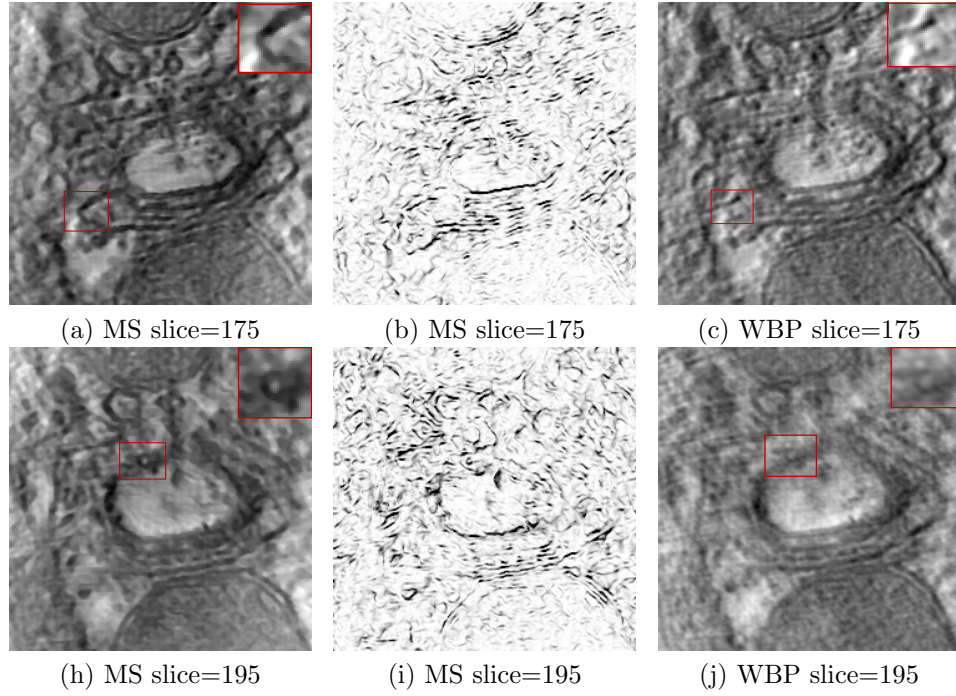


FIGURE 5. Reconstructions of cryo-specimen using the alternating minimization scheme described in Algorithm 3 and artifact reduction strategy in Sec. 2.3. Left column is the reconstructed images, the middle column is the edge sets with our algorithm, and the right column is the reconstructed images with WBP algorithm in TOM toolbox. The images in the red block are zoomed in and put in the top right corner. The edges in the middle column are enhanced in the left column compared to the WBP reconstructions in the right column. Compared to the results of WBP in right column, the results in the left show the effect of noise reduction while the edges are preserved.

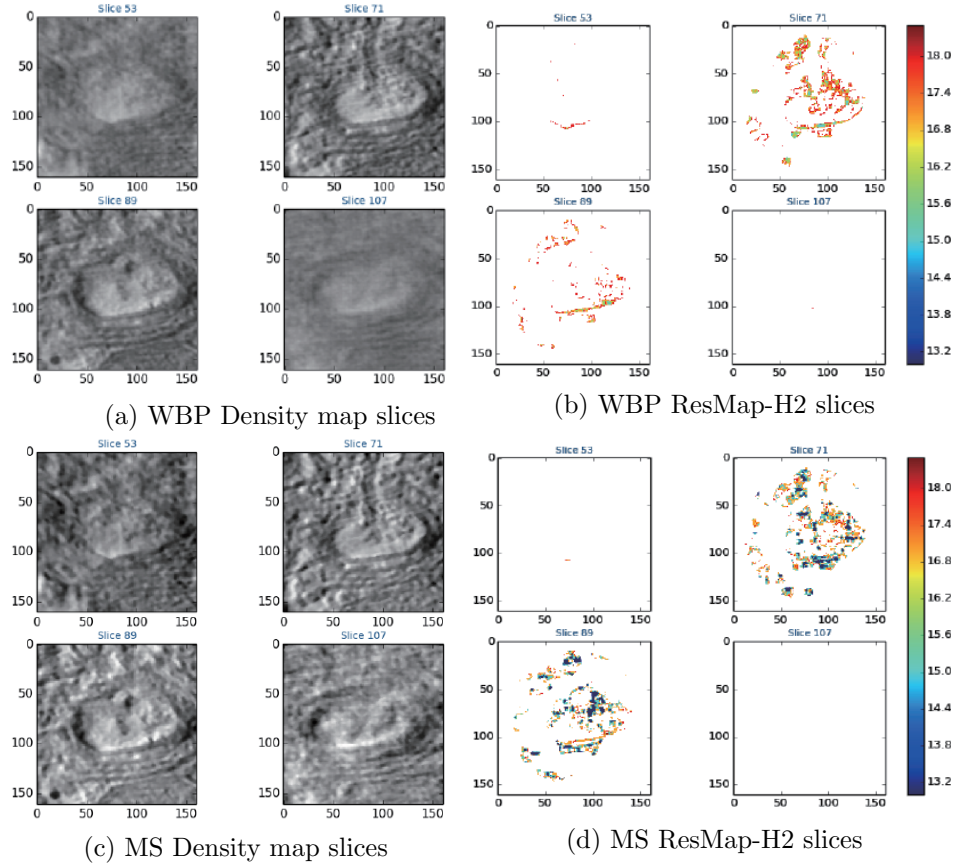


FIGURE 6. Density maps and ResMap of the reconstructed images of WBP method and our method. The mean resolution of WBP is 17.17\AA while the mean resolution of our reconstruction with alternative minimization algorithm is 15.07\AA .

REFERENCES

- [1] Ludwig Reimer. *Transmission electron microscopy : physics of image formation and micro-analysis*. Springer-Verlag, 1989.
- [2] Gabor T. Herman and Joachim Frank. *Computational Methods for Three-Dimensional Microscopy Reconstruction*. Springer New York, 2014.
- [3] D. Fanelli and O. Öktem. Electron tomography: a short overview with an emphasis on the absorption potential model for the forward problem. *Inverse Problems*, 24(1):13001–13051(51), 2008.
- [4] Esther Klann. A mumford-shah-like method for limited data tomography with an application to electron tomography. *SIAM Journal on Imaging Sciences*, 4(4):1029–1048, 2011.
- [5] Jürgen Friel and Eric Todd Quinto. Characterization and reduction of artifacts in limited angle tomography. *Inverse Problems*, 29(12):2091–2128, 2013.
- [6] Stephan Nickell, Friedrich Förster, Alexandros Linaroudis, William Del Net, Florian Beck, Reiner Hegerl, Wolfgang Baumeister, and Jürgen M Plitzko. Tom software toolbox: acquisition and analysis for electron tomography. *Journal of Structural Biology*, 149(149):227–34, 2005.
- [7] H. Rullgård, L.-G. Öfverstedt, S. Masich, B. Daneholt, and O. Öktem. Simulation of transmission electron microscope images of biological specimens. *Journal of Microscopy*, 243(3):234–256, 2011.
- [8] Ozan Öktem. *Handbook of Mathematical Methods in Imaging*, chapter Mathematics of Electron Tomography, pages 937–1031. Springer New York, New York, NY, 2015.
- [9] Michael Radermacher. *Electron Tomography: Methods for Three-Dimensional Visualization of Structures in the Cell*, chapter Weighted Back-projection Methods, pages 245–273. Springer New York, New York, NY, 2006.
- [10] S. Lanzavecchia, F. Cantele, P. L. Bellon, L. Zampighi, M. Kreman, E. Wright, and G. A. Zampighi. Conical tomography of freeze-fracture replicas: a method for the study of integral membrane proteins inserted in phospholipid bilayers. *Journal of Structural Biology*, 149(1):87–98, 2005.
- [11] A. Zampighi Guido, Schietroma Cataldo, M. Zampighi Lorenzo, Woodruff Michael, M. Wright Ernest, and C. Brecha Nicholas. Conical tomography of a ribbon synapse: Structural evidence for vesicle fusion. *Plos One*, 6(3):e16944, 2011.
- [12] Eric Todd Quinto, Ulf Skoglund, and Ozan Oktem. Electron lambda-tomography. *Proceedings of the National Academy of Sciences of the United States of America*, 106(51):21842–7, 2009.
- [13] R. Marabini, E. Rietzel, R. Schroeder, G. T. Herman, and J. M. Carazo. Three-dimensional reconstruction from reduced sets of very noisy images acquired following a single-axis tilt schema: Application of a new three-dimensional reconstruction algorithm and objective comparison with weighted backprojection. *Journal of Structural Biology*, 120(3):363–71, 1998.
- [14] Ronny Ramlau and Wolfgang Ring. Regularization of ill-posed mumfordcshah models with perimeter penalization. *Inverse Problems*, volume 26(26):115001, 2010.
- [15] Erik Sundermann, Filip Jacobs, Mark Christiaens, Bjorn De Sutter, and Ignace Lemahieu. A fast algorithm to calculate the exact radiological path through a pixel or voxel space. *Journal of Computing and Information Technology*, 6(1):89–94, 1998.
- [16] R. L. Siddon. Fast calculation of the exact radiological path for a three-dimensional ct array. *Medical Physics*, 12(2):252–255, 1985.
- [17] Akira Fujimoto, Takayuki Tanaka, and Kansei Iwata. Arts: Accelerated ray-tracing system. *IEEE Computer Graphics and Applications*, 6(4):16–26, 1986.
- [18] Borut Žalik, Gordon Clapworthy, and Črtomir Oblonšek. An efficient code-based voxel-traversing algorithm. *Computer Graphics Forum*, 16(2):119–128, 1997.
- [19] Y. K. Liu, H. Y. Song, and B. Žalik. A general multi-step algorithm for voxel traversing along a line. In *Computer Graphics Forum*, pages 73–80, 2008.
- [20] Joanna Klukowska, Davidi Ran, and Gabor T. Herman. Snark09 c a software package for reconstruction of 2d images from 1d projections. *Computer Methods and Programs in Biomedicine*, 110(3):424–440, 2013.
- [21] D. Mumford and J. Shah. Optimal approximations by piecewise smooth functions and associated variational-problems. *Communications on Pure and Applied Mathematics*, 42(5):577–685, 1989.
- [22] Ming Jiang, Peter Maass, and Thomas Page. Regularizing properties of the mumford-shah functional for imaging applications. *Inverse Problems*, 30(3):1941–1946, 2014.

- [23] Guojie Luo, Ming Jiang, and Peter Maass. Fpga acceleration by asynchronous parallelization for simultaneous image reconstruction and segmentation based on the mumford-shah regularization. 2015.
- [24] L. Ambrosio and V. M. Tortorelli. On the approximation of free discontinuity problems. *Boll. Un. Mat. Ital. B (7)*, 6(1):105–123, 1992.
- [25] Luciano Modica and Stefano Mortola. Un esempio di γ -convergenza. *Bollettino Della Unione Matematica Italiana B*, 5, 1977.
- [26] Andrew R. Webb. *Statistical pattern recognition. 2nd ed.* 2002.
- [27] Silvia Bonettini. Inexact block coordinate descent methods with application to non-negative matrix factorization. *IMA Journal of Numerical Analysis*, 31(4):1431–1452(22), 2011.
- [28] Yoon Mo Jung, Sung Ha Kang, and Jianhong Shen. Multiphase image segmentation via modica-mortola phase transition. *SIAM Journal on Applied Mathematics*, 67(5):1213–1232, 2007.
- [29] Yibao Li and Junseok Kim. Multiphase image segmentation using a phase-field model. *Computers and Mathematics with Applications*, 62(2):737–745, 2011.
- [30] Stephen J. Wright. *Coordinate descent algorithms*. Springer-Verlag New York, Inc., 2015.
- [31] Silvia Bonettini, Marco Prato, and Simone Rebegoldi. *A cyclic block coordinate descent method with generalized gradient projections*. Elsevier Science Inc., 2016.
- [32] J. E. Stone, D. Gohara, and Guochun Shi. Opencl: A parallel programming standard for heterogeneous computing systems. *Computing in Science and Engineering*, 12(3):66–72, 2010.
- [33] A. Munshi. The opencl specification. In *2009 IEEE Hot Chips 21 Symposium (HCS)*, pages 1–314, Aug 2009.
- [34] W. Shang, F. Lu, T. Sun, J. Xu, L. L. Li, Y. Wang, G. Wang, L. Chen, X. Wang, and M. B. Cannell. Imaging ca²⁺ nanosparks in heart with a new targeted biosensor. *Circulation Research*, 114(3):412–20, 2014.
- [35] Huang Xiaohu, Sun Lei, Ji Shuangxi, Zhao Ting, Zhang Wanrui, Xu Jiejia, Zhang Jue, Wang Yanru, Wang Xianhua, Franzini-Armstrong Clara, Zheng Ming, and Cheng Heping. Kissing and nanotunneling mediate intermitochondrial communication in the heart. *Proceedings of the National Academy of Sciences of the United States of America*, 110(8):2846–2851, 2013.
- [36] A Kucukelbir, F. J. Sigworth, and H. D. Tagare. Quantifying the local resolution of cryo-em density maps. *Nature Methods*, 11(1):63–65, 2014.

Received xxxx 20xx; revised xxxx 20xx.

E-mail address: shenli@pku.edu.cn

E-mail address: Todd.Quinto@tufts.edu

E-mail address: wsq@pku.edu.cn

E-mail address: ming-jiang@pku.edu.cn